Composites: Part A 198 (2025) 109157

Contents lists available at ScienceDirect

Composites Part A

journal homepage: www.elsevier.com/locate/compositesa

Modeling and optimization of thermal interface materials featuring horizontally oriented fillers by flow-field driven strategy

Xuan Yang [a], Xinfeng Zhang [a], Tianxu Zhang [a], Linyi Xiang [a], Bin Xie [b,*], Xiaobing Luo [a,*]

[a] School of Energy and Power Engineering, Huazhong University of Science and Technology, Wuhan 430074, China
[b] School of Mechanical Science and Engineering, Huazhong University of Science and Technology, Wuhan 430074, China

HIGHLIGHTS

- Filler orientation in fluid flow was quantified both theoretically and experimentally.
- A novel numerical model for designing and optimizing the filler-oriented fluid-flow field was proposed.
- Thermal conductivity of composite prepared by five-second spin coating was 2.2 times higher than that of randomly oriented composite.
- Mechanism of heat dissipation enhancement by anisotropic filler orientation control was revealed.

ARTICLE INFO

Keywords:
Thermal materials
Filler orientation
Heat dissipation
Flow-field driven

ABSTRACT

Thermal interface materials (TIMs) are essential for electronic thermal management due to their flexibility and high thermal conductivity. Among them, filler-matrix composites are widely used, with filler orientation playing a key role in thermal performance. Shear forces in a fluid flow field effectively align anisotropic, thermally conductive fillers. Here, we developed a numerical model to simulate particle orientation, revealing its dependence on shear rate. A spin-coating strategy, optimized through an analytical model, was employed to fabricate TIMs with horizontally oriented hexagonal boron nitride (hBN). Theoretical analyses of Euler angles, considering spin-coating duration and initial orientation, identified 5 s as the optimal duration for horizontal alignment. Experimental validation using orientation algorithms confirmed the model's accuracy. Thermal conductivity measurements showed that composites produced via this optimized approach achieved 0.92 W m^{-1} K^{-1} at 20 wt % hBN, significantly outperforming randomly oriented composites (0.41 W m^{-1} K^{-1}). This novel orientation strategy and optimization model enhance TIMs' thermal performance, offering a new approach to regulating filler orientation and improving heat-flux control in composite materials.

1. Introduction

Thermal interface materials (TIMs), known for their exceptional flexibility and superior thermal conductivity, have been extensively utilized in the packaging of electronic devices for enhancing the heat transfer across packaging/bonding interfaces [1,2]. TIMs typically consist of polymer matrix with low elastic modulus that is beneficial for filling the air gaps in the thermal interface, and highly thermal-conductive fillers that are pivotal in transporting heat efficiently within the TIMs [3]. To date, a variety of thermal-conductive fillers have been explored, including metal and their oxides (e.g., Al [4] and ZnO_3 [5]), carbon-based materials (e.g., carbon fibers [6] and graphene [7]), and ceramics (e.g., BN [8] and AlN [9]). Notably, many of these fillers exhibit anisotropic thermal properties, i.e., the thermal conductivity in specific direction(s) is superior than that of others [10]. For instance, hexagonal boron nitride (hBN), a kind of platelet-shaped particle, displays an in-plane thermal conductivity of ~ 600W m^{-1} K^{-1}, which is higher than that of through-plane (~30 W m^{-1} K^{-1}). To make full use of such a thermal anisotropy of fillers, it is essential to align the orientation of these fillers with the desired heat dissipation direction [11]. Moreover, regulating the orientation of fillers to suit particular applications may significantly enhance the heat transfer efficiency [12,13]. For instance, in operational chips, there are "hotspot" regions where the temperature is significantly higher than the average temperature of chips. The localized accumulation of heat always causes more rapid aging of the chip [14]. Horizontally oriented hBN could significantly

* Corresponding authors.
E-mail addresses: binxie@hust.edu.cn (B. Xie), luoxb@hust.edu.cn (X. Luo).

https://doi.org/10.1016/j.compositesa.2025.109157
Received 16 March 2025; Received in revised form 18 June 2025; Accepted 1 July 2025
Available online 2 July 2025

enhance the in-plane thermal conductivity of the TIMs, thus improving the thermal management ability towards hotspot in chip.

Following this guideline, considerable researches have developed filler orientation control strategies based on various actuating forces, such as electrical, [15,16] magnetic, [17,18] and shear forces [19,20]. Among them, shear force stands out as the most versatile actuator, which is applicable to all kinds of fillers irrespective of their electrical charge or magnetic properties. In our previous work, we proposed a flow field-driven self-assembly strategy to fabricate oriented and centrosymmetric composites, [21] and the dynamics of filler orientation in a polymer fluid were extensively analyzed [22]. It has been experimentally demonstrated that shear forces could induce CFs to rotate and orient along the streamlines. However, the fillers' orientation dynamics in the flow field has not been explored yet. In the meantime, considering the divergent initial distributions and orientation conditions of these fillers, an optimization criterion is highly needed for guiding the design and fabrication of fillers' microstructures.

To tackle with this issue, here we developed a numerical model that the fluid containing microparticles is regarded as a homogeneous equivalent fluid, and the interactions with the rigid particles embedded within are quantified by considering the temporally varying velocity gradient of this equivalent fluid, to describe the filler orientation dynamics in flow field. A critical indicator, horizontal orientation proportion (HOP), was proposed to quantitively evaluate the optimal flowing-rotating duration in the spin coating-based fabrication process of TIMs. An orientation algorithm based on microscale image identification was employed to determine fillers' angular distribution in the matrix, confirming the predictions of the numerical model. Fig. 1a and b schematically illustrate the orientation process of the fillers during the spin-coating procedure. It shows that hBN particles rotate in the flow field generated by the spinning fluid. The HOP of the platelets for coating durations of 5, 10, and 15 s were systematically quantified. According to the model, the optimal spin-coating duration was identified as 5 s, achieving a HOP-5 (orientation within the range of 0 ~ 5° and 175 ~ 180°) of 67.90 %, which was significantly higher than the 41.98 % and 50.62 % observed at 10 and 15 s, respectively. The measured thermal conductivities of the samples revealed that the highest conductivity of 0.92 W m^{-1} K^{-1} was achieved in the composite prepared with a five-second spin coating duration, which is considerably higher than 0.41W m^{-1} K^{-1} of the randomly oriented composite. This methodology facilitates the precise orientation control towards thermal fillers in polymer matrix, which is promising in the targeted design and fabrication of high-performance TIMs.

2. Numerical model

2.1. Particle rotation dynamics

The mixture of hBN (with an average diameter of 45 μ m) and polydimethylsiloxane (PDMS) is considered as a homogeneous incompressible Newtonian fluid. The orientation vector **p** of the particle follows the Jeffery equation: [23]

$$\dot{\mathbf{p}} = \boldsymbol{\omega}\cdot\mathbf{p} + \lambda(\mathbf{E}\cdot\mathbf{p} - \mathbf{E} : \mathbf{ppp}) \tag{1}$$

where **ω** is the vorticity tensor and **E** is the deformation rate tensor, respectively. They are calculated by the velocity gradient ∇**v**:

$$\boldsymbol{\omega} = \left(\nabla\mathbf{v}^{\mathrm{T}} - \nabla\mathbf{v}\right)/2 \tag{2}$$

$$\mathbf{E} = \left(\nabla\mathbf{v}^{\mathrm{T}} + \nabla\mathbf{v}\right)/2 \tag{3}$$

where λ is the shape factor and is defined as:

$$\lambda = \left(r_c^2 - 1\right)/\left(r_c^2 + 1\right) \tag{4}$$

where r_c is the aspect ratio. For rod-shaped particle with long length and small diameter, λ tends to be 1, and for thin disc-shaped particle, λ tends to be − 1. To simplify the description, **p** is represented in spherical coordinate system through Euler angles as θ and ϕ, as shown in Fig. 1c. Due to the symmetry of the disc-shaped particle, there is no distinction between the top and bottom surfaces of the disc. θ and ϕ are equal to π–θ and π–ϕ, respectively. Applying transformation relation: $p_x = \sin\theta\cos\phi$, $p_y = \sin\theta\sin\phi$ and $p_z = \cos\theta$, and substituting Eq. (2) and (3) into Eq. (1), the time-dependent evolution expression of θ and ϕ are obtained as follows:

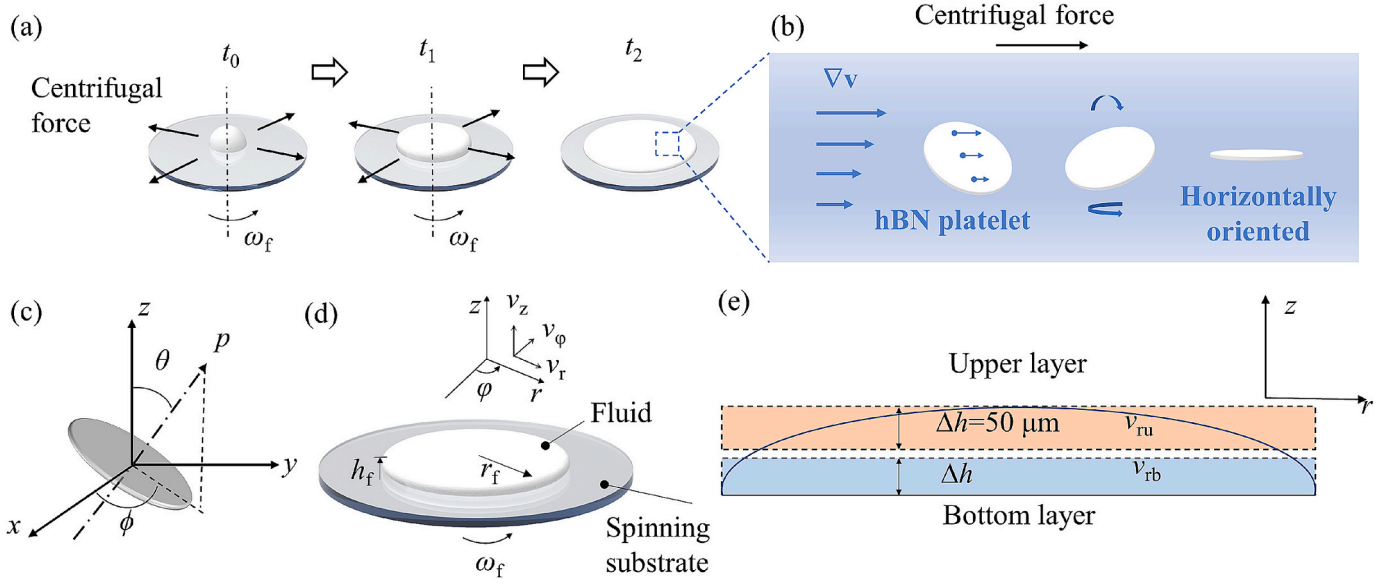

Fig. 1. Schematic of spin coating process and the numerical model. (a) Fluid flow under centrifugal force (b) Filler's orientation within the fluid. (c) Schematic of disc-shaped particle direction vector in spherical coordinate system. p is the orientation vector of particle. θ is the angle between orientation vector p and the z-axis. ϕ is angle between x-axis and the projection of vector p onto the x-y plane. (d) Fluid flow in spin coating process. v_z, v_φ, and v_r are the the velocity in radial, circumferential, and axial direction, r_f and h_f are the radius and thickness of the fluid, respectively. ω_f is the angular velocity of the spinning substrate. (e) Schematic showing the two-layer model in r-z plane. The thickness of each layer is Δh = 50 μm. v_{ru} and v_{rb} are the radial velocity of the particles in each layer, respectively.

$$\dot{\theta}^k = \omega_{31}^k \cos\phi^k + \omega_{32}^k \sin\phi^k + \frac{\lambda}{4}\left[\left(E_{11}^k + E_{22}^k - 2E_{33}^k\right)\sin 2\theta^k + \left(E_{11}^k - E_{22}^k\right)\sin 2\theta^k \cos 2\phi^k + 2E_{12}^k \sin 2\theta^k \sin 2\phi^k + 4\left(E_{13}^k \cos\phi^k + E_{23}^k \sin\phi^k\right)\cos 2\theta^k\right] \quad (5)$$

$$\dot{\phi}^k = \omega_{12}^k + \omega_{13}^k \frac{\cos\theta^k}{\sin\theta^k}\sin\phi^k - \omega_{23}^k \frac{\cos\theta^k}{\sin\theta^k}\cos\phi^k + \lambda\left[E_{12}^k \cos 2\phi^k + \frac{E_{22}^k - E_{11}^k}{2}\sin 2\phi^k + \left(E_{23}^k \cos\phi^k - E_{13}^k \sin\phi^k\right)\frac{\cos\theta^k}{\sin\theta^k}\right] \quad (6)$$

where superscript k is the time.

2.2. Fluid flow during spin coating

The velocity field during spin coating is solved in a cylindrical coordinate system. Fig. 1d shows the spin coating process: v_r, v_φ, and v_z are the velocity in radial, circumferential, and axial direction, r_f and h_f are the radius and thickness of the fluid, respectively. ω_f is the angular velocity of the spinning substrate. Since the flow process occurs mainly in the radial direction, $\nabla\mathbf{v}$ is simplified as:

$$\nabla\mathbf{v}(r,\varphi,z) = \begin{bmatrix} \partial v_r/\partial r & 0 & \partial v_r/\partial z \\ 0 & v_r/r & 0 \\ 0 & 0 & -(\partial v_r/\partial r + v_r/r) \end{bmatrix} \quad (7)$$

The radial velocity v_r is calculated as: [24]

$$v_r = \left(-0.5\rho\omega_f^2 r_f z^2 + \rho\omega_f^2 r_f h_f z\right)/\mu \quad (8)$$

where μ and ρ are dynamic viscosity and density of the fluid, respectively. h_f and r_f can be expressed as follows:

$$h_f = \frac{h_0}{\left(1 + \frac{4\rho\omega_f^2 h_0^2 t}{3\mu}\right)^{0.5}} \quad (9)$$

$$r_f = r_0\left(1 + \frac{4\rho\omega_f^2 h_0^2 t}{3\mu}\right)^{0.75} \quad (10)$$

where h_0 and r_0 are thickness and radius at $t = 0$, respectively. The parameters used for the calculations are listed in Table 1.

A two-layer model was proposed to study the orientation of hBN. In the upper layer, the flow of fluid is relatively strong thus v_r, $\partial v_r/\partial r$, and $\partial v_r/\partial z$ exist simultaneously. In the bottom layer, due to the viscous interaction between the fluid and the wall, $v_r = 0$ and there is only $\partial v_r/\partial z$. To simplify the calculation, the upper layer was defined as a fluid layer with thickness of 50 μ m (slightly exceeding the diameter of hBN) from the upper to down. Similarly, the bottom layer is designated as a fluid layer extending upward from the substrate, also measuring 50 μ m in thickness. Fig. 1e illustrates this two-layer conceptual model. Within this framework, the hBN particles are monitored separately in both layers. In the upper layer, due to time-dependent nature of v_r and r_{fu}, the orientation dynamics of three representative particles with specific initial radial coordinates are examined. In the bottom layer, the radial coordinates of the particles remain constant, while the shear rate varies with both radial coordinate and time, necessitating the investigation of the orientation dynamics of three representative particles at fixed positions.

Table 1
Parameters used for calculation.

Parameter	Symbol	Value
Density of the fluid mixture	ρ	1030 kg m^{-3}
Dynamic viscosity	μ	3.5 kg m^{-1} s^{-1}
Diameter of hBN platelets	d	45 μm
Aspect ratio	r_c	0.05

The velocity gradient in the upper layer are calculated as follows:

$$\partial v_{ru}/\partial r = \left[v_{ru}\left(r_{fu}, h_{fu}\right) - v_{ru}\left(r_{fu} - \Delta r_f, h_{fu}\right)\right]/\Delta r_f \quad (11)$$

$$\partial v_{ru}/\partial z = \left[\left(r_{fu}, h_{fu}\right) - v_{ru}\left(r_{fu}, h_{fu} - \Delta h\right)\right]/\Delta h \quad (12)$$

and in the bottom layer:

$$\partial v_{rb}/\partial z = v_{rb}\left(r_{fb}, h_{fb}\right)/\Delta h \quad (13)$$

where v_{ru} and v_{rb} are the radial velocities, r_{fu} and r_{fb} are the radial coordinates, and h_{fu} and h_{fb} are z-axis coordinates of the tracked hBN particles in upper and bottom layers, respectively. It should be noted that v_{rb} is adopted to calculate the shear rate in the bottom layer, and the radial velocity of the particles in the bottom layer is still considered to be zero.

3. Materials and experiments

Hexagonal boron nitride (hBN) platelets with an average diameter of 45 μ m (Momentive) and PDMS matrix (Sylgard 184, Dow Corning) were mixed to fabricate the composite fluids. The mass fractions of hBN were controlled at levels of 5 wt%, 10 wt%, 15 wt% and 20 wt% across different samples. Prior to use, these composite fluids underwent a vacuum-based degassing treatment to remove air bubbles, ensuring the purity and uniformity of the mixtures. For the spin coating process, a drop of the degassed fluid was initially placed at the center of a spinning substrate with a 12.5 mm radius, forming a hemisphere with a radius of approximately 3 mm. This substrate was then spun at a speed of 2000 rpm for durations of 5, 10, and 15 s to produce films of varying characteristics. Subsequent to the spin coating, the films were cured at 100 °C for 5 min. To obtain films of different thicknesses, this procedure could be repeated as needed, allowing for precise control over the film dimensions and properties.

Scanning electron microscope (SEM) images of hBN-PDMS composites were obtained by a field-emission SEM (Sirion 200, Netherlands). The in-plane and through-plane thermal diffusivity α of hBN-PDMS composites were measured through a laser flash analysis (LFA457, Nezsch). Specific heat capacity C_p of the samples were obtained by a differential scanning calorimetry (Diamond DSC, PerkinElmer). Density ρ of the samples were tested by an electron density meter (XF-220SD, LICHEN). Thermal conductivity κ of the samples were calculated through $\kappa = \alpha \cdot C_p \cdot \rho$. Surface temperature of the samples were measured by a thermal infrared imager (SC620, FLIR).

4. Results and discussion

Due to the rigidity of hBN platelet, the velocity gradient within the fluid medium induces rotational motion in these platelets when exposed to shear forces. In the context of purely shear-driven flow fields, Eqs. (5) and (6) are calculated as follows:

for $\partial u/\partial y = 1$,

$$\dot{\theta}^k = 0.25\lambda \sin 2\theta^k \sin 2\phi^k \quad (14)$$

$$\dot{\phi}^k = -0.5 + 0.5\lambda \cos 2\phi^k \quad (15)$$

for $\partial u/\partial z = 1$,

$$\dot{\theta}^k = \left(0.5 + 0.5\lambda \cos 2\theta^k\right)\cos\phi^k \quad (16)$$

$$\dot{\phi}^k = -0.5(\lambda + 1)\frac{\cos\theta^k}{\sin\theta^k}\sin\phi^k \quad (17)$$

according to Eqs. (14) and (15), the rate of angular change approaches

0 at (θ, ϕ)= (0°, 90°) or (90°, 90°) for a disc-shaped hBN particle with a shape factor λ tends to be − 1. This indicates that the particle will rotate at a markedly slow speed when its angle (θ, ϕ) is close to (0°, 90°) defined as S1 or (90°, 90°) defined as S2, suggesting relatively stable states of horizontal and vertical orientation, respectively. Conversely, Eqs. (16) and (17) indicate relatively stable states of vertical and horizontal orientation when (θ, ϕ) is at (0°, 0°) or (90°, 90°). Fig. 2a and b show the stable states in flow field with shear rate in x-y or x-z plane. In the stable state, the particle's projected area in the direction perpendicular to the fluid flow (A_u) is minimized. Coupled with the huge aspect ratio, it results in zero torque M_o (torque out of the direction of orientation vector p of the particle) exerted on the particle, thereby the particle only rotates along its own orientation vector p under the effect of M_i (torque in the direction of p). Fig. 2c-f investigates the M_o exerted on the particles when their A_u increase in flow field with shear rate in x-y and x-z planes, respectively. In x-y plane, with the shear effect of $\partial u/\partial y$, when the particle's A_u increased from the stable state S1 to ($\theta = 30°$, $\phi = 0°$), the M_o generated by $\partial u/\partial y$ made the particle rotate as Fig. 2c illustrated, indicating that the particle in state S1 could not return to its initial stable state under shear effect $\partial u/\partial y$, after being disturbed in the flow field. In contrast, the particle in state S2 could return to S2 through the generated M_o by $\partial u/\partial y$, as shown in Fig. 2d. The above analysis revealed that in the flow filed with shear effect $\partial u/\partial y$, hBN particle tends to be stay stable in a vertical orientation of ($\theta = 90°$, $\phi = 90°$). Analyzing the particle in flow field with shear effect $\partial u/\partial z$ in Fig. 2e and f in the same way, it can be obtained that hBN particle tends to be stay stable in a horizontal orientation of ($\theta = 0°$, $\phi = 0°$) under shear effect of $\partial u/\partial z$. Thus, to achieve horizontal orientation of hBN, a flow field characterized by a shear rate of $\partial u/\partial z$ is necessary.

Spin coating, a technique widely employed for the fabrication of thin films, leverages the centrifugal force generated by the rotation of the substrate. Comparing to other orientation strategy, spin-coating is mature and easy-to-operate, non-destructive to the material, and wide compatibility with no special requirements for the matrix. Attributed to the fluid viscosity and the no-slip boundary condition as the wall, a velocity gradient can be created in the vertical direction during the spin coating process. As the fluid at the center flows radially, it forms a uniform film while simultaneously orients the fillers within it by the velocity gradient in the vertical direction. This mechanism can be effectively utilized to orient hBN particles horizontally within the film matrix. Fig. 3a illustrates the initial thickness-radius distribution of the fluid, which is depicted as a Gaussian-shaped r_0-h_0 curve. At the center of the substrate, the fluid began with a thickness of 3 mm and tapered off to 0 at $r_0 = 5$ mm. Fig. 3b shows the changes in maximum thickness h_{fmax} and radius r_{fmax} of the fluid at different moments under an angular velocity $\omega_f = 209.44\times(1 - e^{-1.5t})$. Initially, h_{fmax} rapidly decreased from 3 mm to 0.18 mm within the first two seconds, and then continued to diminish more gradually, reaching 0.06 mm at 15 s. Concurrently, r_{fmax} exhibited a nearly uniform expansion from 5 mm to 234.20 mm over the same duration. Given the rapid uniformity achieved via spin coating, h_{fmax} was adopted as the representative thickness across all radial coordinates. Three hBN platelets were tracked both in upper and bottom layer, respectively. At the initial time ($t = 0$ s), the radial coordinates of the three hBN particles in the upper layer were noted at 0.1 mm, 0.4 mm, and 1.2 mm, respectively. In contrast, the fixed radial coordinates in the bottom layer were set as 2 mm, 10 mm, and 100 mm, respectively. This configuration allowed for the detailed observation of the hBN platelets' orientation behavior under varying conditions throughout the spin coating process.

Fig. 3c-d illustrate the dynamic evolution of particle movement within the upper layer during a fifteen-second spin coating process. As shown in Fig. 3c, the radial coordinates of the tracked particles experienced significant increases, reaching final distances of 33.3 mm, 126.1 mm, and 234.2 mm at $t = 15$ s. This rapid expansion in radial coordinates correlated with the increasing rotational speed of the substrate during the initial phase of spin coating. Fig. 3d captures the behavior of the radial velocity of these particles, which increased rapidly in the first two seconds due to both the increasing rotation speed of the substrate and the expanding radial coordinates. After this initial surge, the radial velocity then gradually declined over the remainder of the period, which was mainly due to the substantial reduction in fluid thickness. Additionally, the derivative $\partial v_{ru}/\partial z$ demonstrated a consistent increase over time, indicating an intensified shearing effect within the upper layer. Notably, particles starting at larger initial radial coordinates displayed a

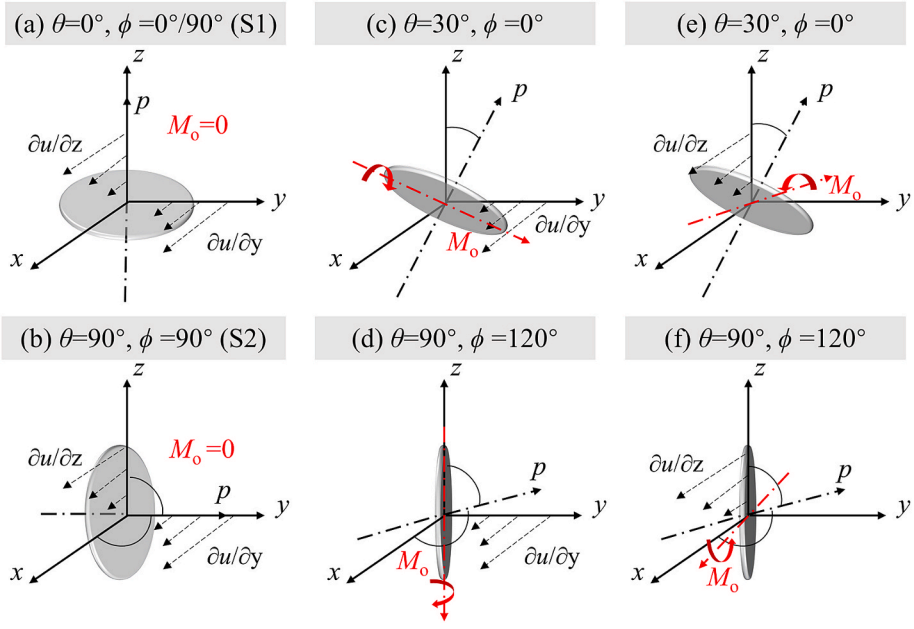

Fig. 2. Torques out of the direction of orientation vector p (M_o) exerted on the particles by purely shear-driven flow fields. $\partial u/\partial y$ and $\partial u/\partial z$ are the shear rate in x-y and x-z plane, respectively. Particles of (a) $\theta = 0°$, $\phi = 0°$ or 90° and (b) $\theta = 90°$, $\phi = 90°$ in flow field with shear rate in x-y or x-z plane. Particles of (c) $\theta = 30°$, $\phi = 0°$ and (d) $\theta = 90°$, $\phi = 120°$ in flow field with shear rate in x-y plane. Particles of (e) $\theta = 30°$, $\phi = 0°$ and (f) $\theta = 90°$, $\phi = 120°$ in flow field with shear rate in x-z plane.

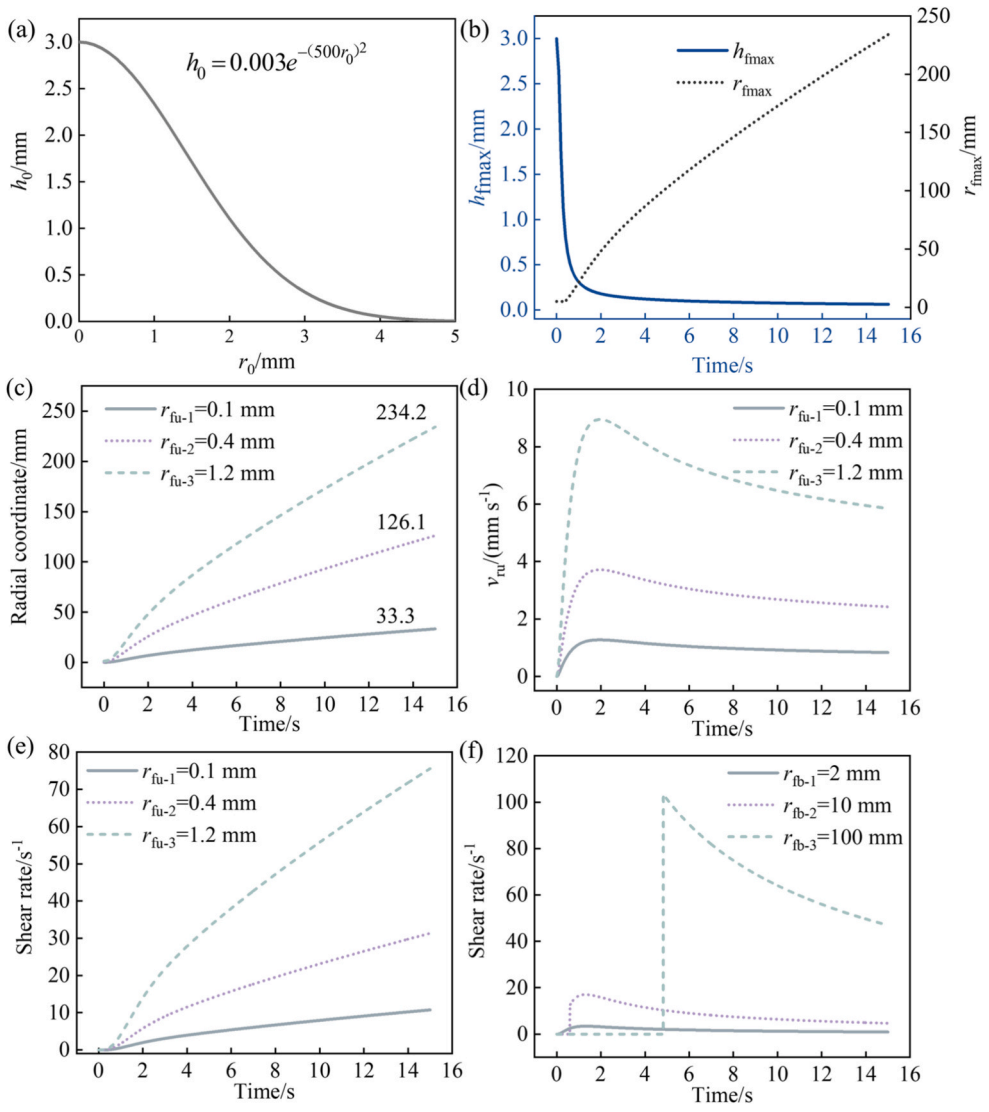

Fig. 3. Evolution of the fluid and the particle movement during a fifteen-second spin coating process. (a) Initial thickness h_0 and radius r_0 distribution of the fluid. (b) Maximum thickness h_{fmax} and radius r_{fmax} of the fluid at different moments. (c) Radial coordinates of the tracked hBN particles at different time. (d) Radial velocity v_{ru} of the tracked particles in the upper layer at different time. (e) Shear rate $\partial v_{ru}/\partial z$ of the tracked particles in the upper layer at different time. r_{fu-1}, r_{fu-2} and r_{fu-3} are the radial coordinates of the tracked hBN particle in upper layer at $t = 0$ s, respectively. (f) Shear rate $\partial v_{rb}/\partial z$ of the tracked particles in the bottom layer. r_{fb-1}, r_{fb-2} and r_{fb-3} are the radial coordinates of the tracked hBN particle in bottom layer at $t = 0$ s, respectively.

quicker acceleration in their radial coordinate, radial velocity, and shear rate. This phenomenon was primarily attributed to the centrifugal force $F = m\omega_f^2 r_f$, which escalated with radius, amplifying these effects at greater distances from the center. Fig. 3e examines $\partial v_{rb}/\partial z$ in the bottom layer at various times, revealing significantly higher values at larger radial coordinates compared to smaller ones. During the early stages of spin coating, as the fluid has yet to extend to the outer radius, the values at these locations were zero. Different from $\partial v_{ru}/\partial z$ in the upper layer, $\partial v_{rb}/\partial z$ in the bottom layer diminished over time due to the decreasing thickness of the fluid, which consequently reduced the shearing effect as the process progresses. This comprehensive analysis underscored the differential dynamics experienced by particles in distinct layers of the spin coating environment, governed by their respective radial positions and the evolving physical conditions of the fluid medium.

Fig. 4 delves into the angular variation of particles within the fluid, starting at initial angles with $\phi_0 = 30°$ and $\theta_0 = 30°$. Influenced by the shearing effect $\partial v_{ru}/\partial z$ in the r-z plane, θ exhibits periodically variations while ϕ oscillated within a specific range. This behavior indicated that the particles rotated along the radial direction and swung in the orthogonal direction. This dual motion pattern was further decomposed in Fig. 4g and h. For the disc-shaped particles analyzed in this study, achieving a horizontal orientation was characterized by θ reaching 0° or 180°. Subsequent analyses, therefore, focus on the evolution of θ. During the spin coating process, one complete rotation period consisted of an equilibrium state where θ was either 0° or 180° (indicating horizontal orientation), and a rotation process where θ varied. Notably, the equilibrium state generally occupied a larger portion of the rotation period compared to the rotation process. Additionally, as the radial coordinates increased, both in the upper and bottom layers, the duration of the rotation period shortened, and the proportion of time that particles spent in the equilibrium state during each period also diminished. This is mainly due to an increase in shear rate with radius, as depicted in Fig. 3e and f, resulting in greater shear forces that increase the rotation speed of the particles. In the upper layer, the increased particle radial coordinates over time accelerated the decrease of the length of rotation period. Conversely, in the bottom layer, while radial coordinates were fixed, decreasing thickness of the fluid over time reduced v_r and $\partial v_r/\partial z$, consequently shortening the rotation period. Achieving a longer equilibrium state within each rotation period is crucial for maintaining horizontal orientation of the particles. According to above analysis, this

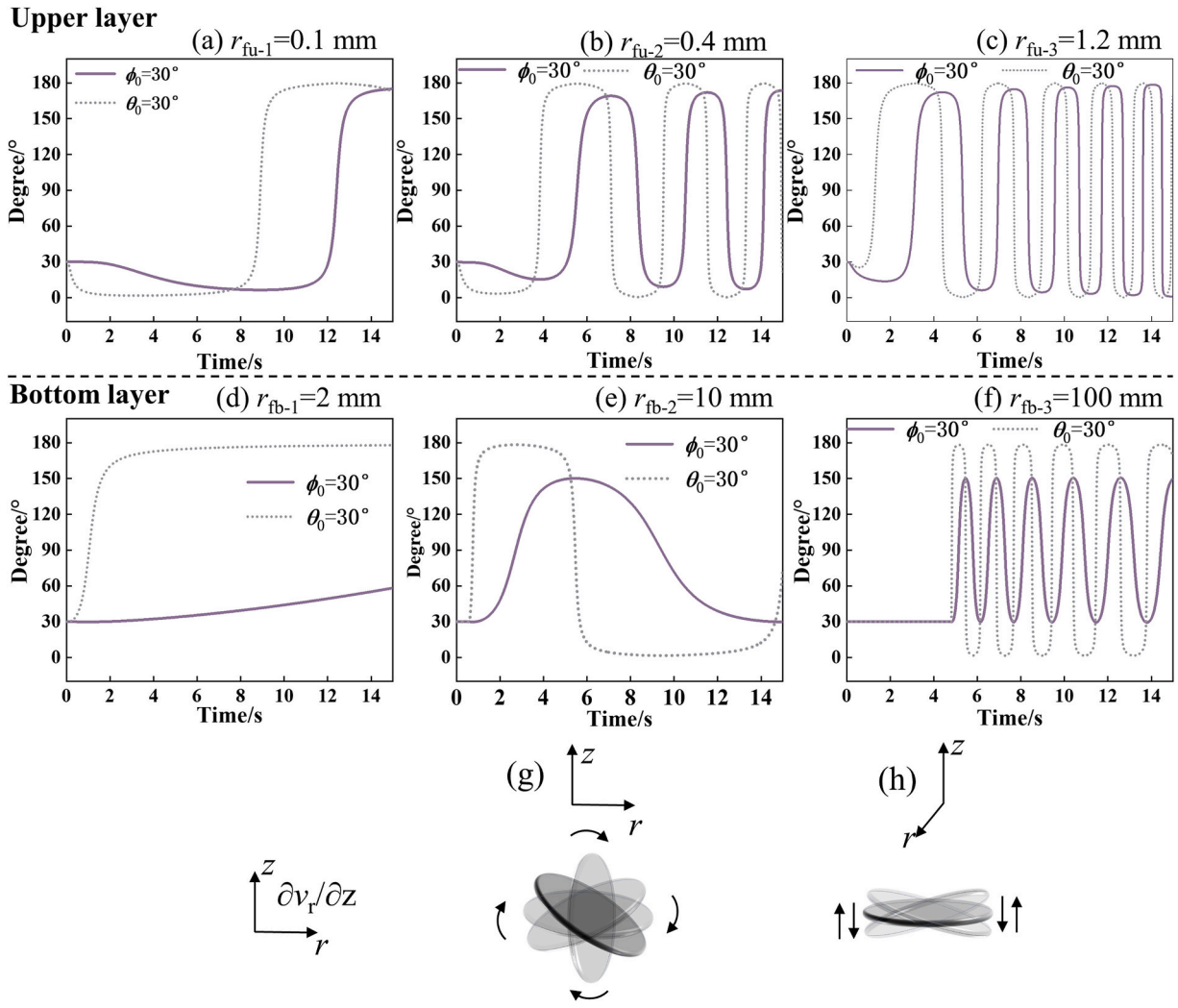

Fig. 4. Time-dependent evolution of ϕ and θ of different particles with $\phi_0 = 30°$ and $\theta_0 = 30°$ in the fluid. (a)-(c) show the particle with initial radial positions of 0.1 mm, 0.4 mm, and 1.2 mm in upper layer, respectively. (d)-(f) show the particle with radial positions of 2 mm, 10 mm, and 100 mm in bottom layer, respectively. (g) Particle rolling along the radial direction and (h) swinging in the other direction.

demands a relatively low shear rate. However, reducing the spin substrate's rotation speed to lower the shear rate is not feasible without sacrificing the uniformity of the fluid layer. Instead, optimizing the duration of the spin-coating process to ensure that most particles spend a majority of the time in the equilibrium state becomes a more practical approach.

During the spin coating process, the fluid was propelled radially under the influence of centrifugal force, leading to a transition of the fluid in the upper layer from a smaller to a larger radius. For instance, it is seen from Fig. 5a that a particle with an initial radial position of 0.1 mm in the upper layer moved to 33.3 mm in 15 s, covering the entire radius of the 12.5 mm substrate. This movement allows us to trace the orientation changes of this particular particle, thus providing insights into the general behavior of particles during spin coating. According to the symmetry, particles' orientation with a series of initial θ (10°, 20°, 30°, 40°, 50°, 60°, 70°, 80°, 90°) and ϕ (10°, 20°, 30°, 40°, 50°, 60°, 70°, 80°, 90°) were studied across various operational durations (5, 10, and 15 s). Fig. 5a displays the initial orientations of 81 particles with different initial Euler angles. The value of θ, represented by polar angle, indicates the degree of horizontal orientation, i.e., the closer a data point is to the 0-180° axis at the bottom, the more horizontally oriented the particle. Subsequent observations revealed that after the spin coating, the θ values of most particles are closed to 0° or 180° due to the shearing effect in r-z plane indicative of a significant shift toward horizontal orientation. Fig. 5b demonstrates the θ distribution after a five-second spin coating, highlighting a predominant aggregation around the 0-180° axis, primarily within the ranges of 0 ~ 10° and 170 ~ 180°. Fig. 5c, which maps the θ distribution after ten seconds, shows particles within the range of 150 ~ 180°. Fig. 5d shows the θ distribution from a fifteen-second spin coating, while most particles remained within the range of 0 ~ 10° and 170 ~ 180°, the clustering near the 0-180° axis was less marked compared to the five-second scenario. To quantify these observations, the horizontal orientation proportion (HOP) for θ within the ranges of 0 ~ 2° and 178 ~ 180° (HOP-2), and 0 ~ 5° and 175 ~ 180° (HOP-5) were calculated for each case. Comparative analysis presented in Fig. 5e illustrates that the HOP-2 and HOP-5 were 29.63 % and 67.90 % respectively after five seconds of spin coating. These values were 12.35 % and 41.98 % after ten seconds, and 17.28 % and 50.62 % after fifteen seconds. The underlying mechanism appears to be linked both the decreasing rotation period and proportion of equilibrium state within each rotation period at greater radial coordinate over time, as depicted in Fig. 3c and Fig. 4a-c. The extended spin process resulted in a reduced duration that particles maintained in a horizontal orientation. Thus, for particles with diverse initial orientations, the probability that particles simultaneously stayed in equilibrium state is reduced in longer spin coating processes, manifested as a decrease in the value of HOP. These results indicate that a five-second spin coating duration yields the optimal horizontal orientation of particles.

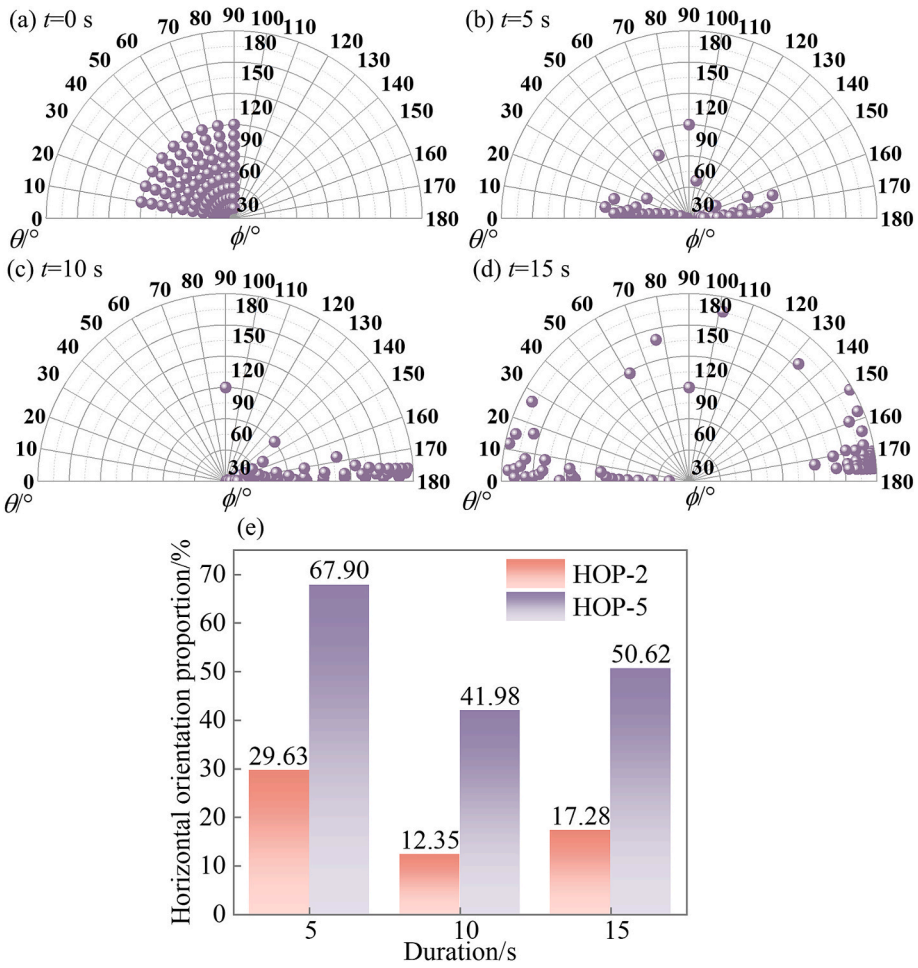

Fig. 5. Numerical analysis of filler orientation in spin coating with duration of 5, 10 and 15 s. Distribution of ϕ and θ of particles at (a) $t = 0$ s, (b) $t = 5$ s, (c) $t = 10$ s, and (d) $t = 15$ s. The polar radius is the value of ϕ and the polar angle is the value of θ. (e) HOP of the particles after five-, ten-, and fifteen- second spin coating, respectively.

Fig. 6a-d illustrate scanning electron microscope (SEM) images of different composites comprising 20 wt% of hBN prepared through both random orientation and controlled spin coating durations of five, ten, and fifteen seconds. These images reveal uniform embedding of hBN platelets within the PDMS matrix, and there were also some cavities which were formed by lost hBN platelets during the tested sample preparetion for SEM analysis. These cavities, alongside the intact platelets, facilitate the assessment of particle orientation within the composite. In Fig. 6a, the orientation of particles appears disordered, with both platelets and resultant cavities oriented in various directions. In contrast, Fig. 6b-d illustrate a pronounced horizontal orientation of particles, underscoring the efficacy of spin coating in manipulating particle orientation. To quantitatively evaluate the orientation of particles within these composites, an orientation algorithm based on microscale image identification developed in our previous work was utilized [25]. The angle distributions derived from this method are depicted in Fig. 6e-h. The composite with randomly oriented particles exhibited a relatively uniform distribution of angles across the $0 \sim 180^\circ$ range. Conversely, the distributions for the spin-coated composites were significantly skewed towards 0° and 180°, with the composite subjected to five seconds of spin coating showing the highest proportion of particles closely aligned to these angles. Fig. 7a presents the HOP for angles within 5° and 10° of the horizontal (HOP-5 and HOP-10) of the experimentally prepaerd composites. They were 1.29 % and 7.53 % for randomly oriented, 9.68 % and 26.59 % for five-second spin coating, 4.88 % and 17.26 % for ten-second, 6.86 % and 22.65 % for fifteen-second. These findings suggest that the optimal horizontal orientation of particles is achieved with a five-second spin coating, followed sequentially by fifteen-second, ten-second, and random orientation. This order of efficacy confirms the predictions of previous modeling and validates the model's accuracy. Nevertheless, the experimental HOP were observed to be lower than those predicted in Fig. 5e. This discrepancy may be attributed to several factors: 1) The orientation analysis performed by the microscale image identification algorithm captures two-dimensional orientation data, whereas the model calculates three-dimensional orientation. 2) Differences between the initial angle distributions used in the experimental setup and those assumed in the simulations. 3) Particle migration to the substrate surface during fluid spreading, where they may be subject to significant shearing forces, potentially altering their orientation. 4) Effects of particle interactions. Fig. 7b and c compares the structures of the filler from edge to center of within the sample of 20 wt% hBN prepared by five-second spin coating. Generally, there were no obvious differences between the different locations (I, II, III, and IV). Only fillers at location I showed a slightly lower proportion of angles around 10° than others, revealing that the filler structures were the same from the center to edge within the samples.

Heat dissipation ability of hBN incorporated TIMs is highly related to the orientation of hBN. Fig. 8a shows a hBN partilce with anisotropic thermal conductivity of out-plane κ_o and in-plane κ_i (dominant heat-dissipation direction), and a temperature gradient $\partial T/\partial n$, represented by a direction vector n, which forms an angle β with κ_i. The heat flux in out-plane q_o and in-plane q_i direction are as follows:

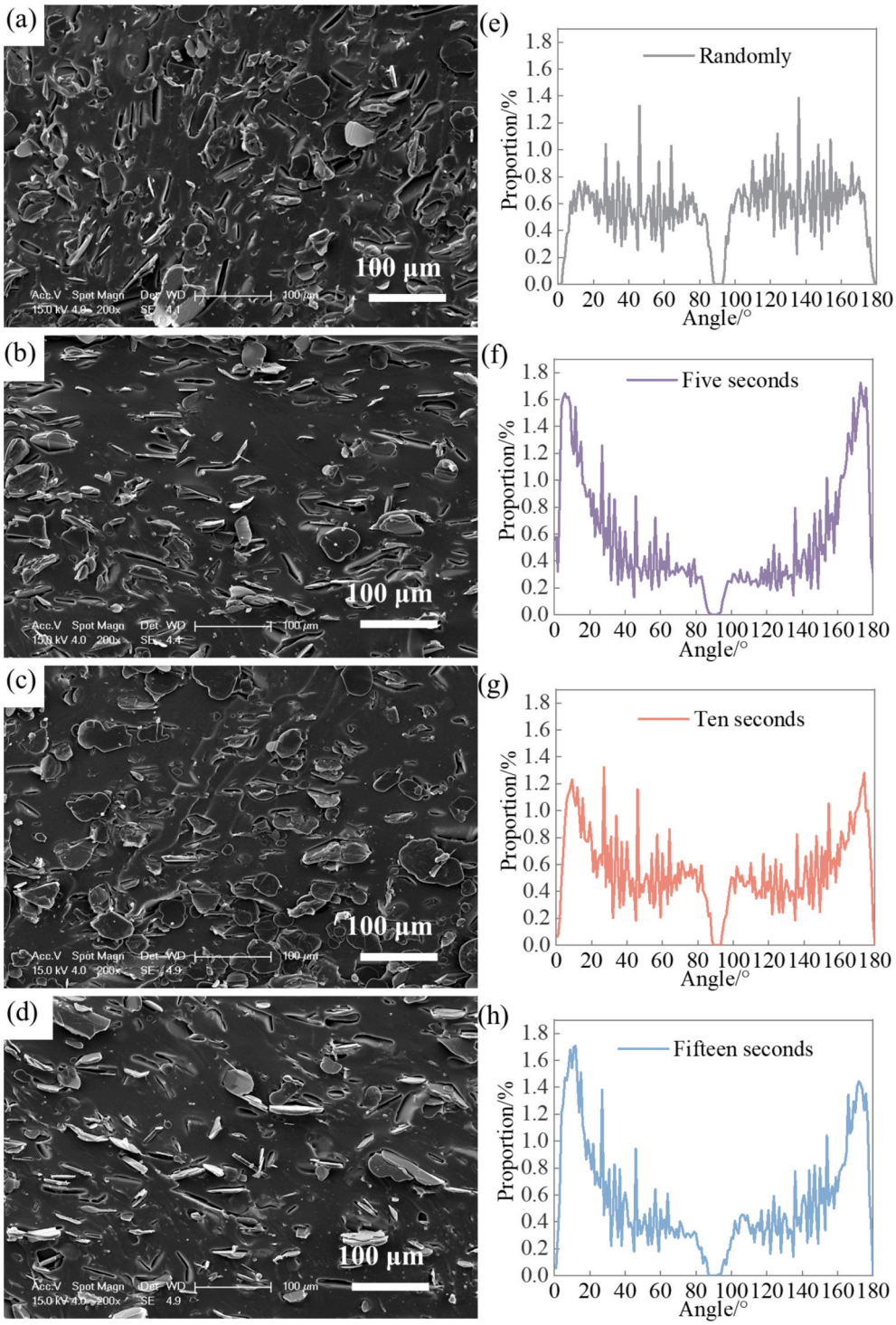

Fig. 6. Experimental analysis of filler orientation in spin coating. SEM images of different composites prepared by (a) randomly oriented, (b) five-second spin coating, (c) ten-second spin coating, and (d) fifteen-second spin coating. (e)-(h) are the corresponding angular distributions of fillers in (a)-(d), respectively.

$$q_o = \kappa_o \cdot \partial T/\partial n \cdot \sin\beta \tag{18}$$

$$q_i = -\kappa_i \cdot \partial T/\partial n \cdot \cos\beta \tag{19}$$

and the overall heat flux q in the particle is:

$$q = \sqrt{q_o^2 + q_i^2} = \partial T/\partial n \cdot \sqrt{(\kappa_i^2 - \kappa_o^2)\cos^2\beta + \kappa_o^2} \tag{20}$$

From Eq. (20), it can be obtained that q attains its maximum value, $q{=}\partial T/\partial n \cdot \kappa_i$, at $\beta = 0°$ or 180°. This indicates that the heat dissipation capacity is maximized when the in-plane orientation of hBN aligns with the temperature gradient.

A two-dimensional finite element method (FEM) was employed to study the heat-flux manipulating ability of composites with horizontally oriented hBN particles (composite-H). Fig. 8b-e display the comparative analysis of temperature and heat flux distributions between composites with randomly oriented hBN (composite-R) and composite-H. In the simulation, a 50 W heat source was applied to the right side of the composites, while a heat convection coefficient of 100 W m^{-2} K^{-1} was

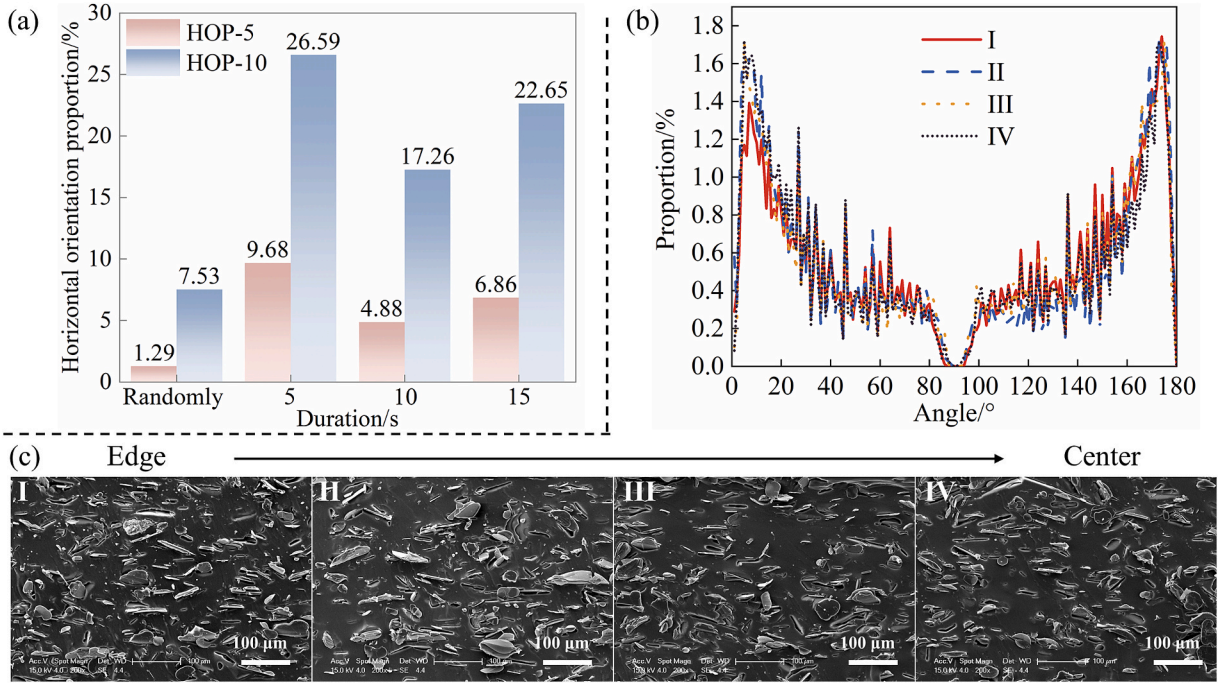

Fig. 7. (a) HOP of the composites prepared by randomly oriented, five-, ten-, and fifteen- second spin coating. (b) Angular distributions of the fillers at different locations (I, II, III, IV) from edge to center within the samples of 20 wt% hBN prepared by five-second spin coating. (c) Corresponding SEM images of the fillers from edge to center.

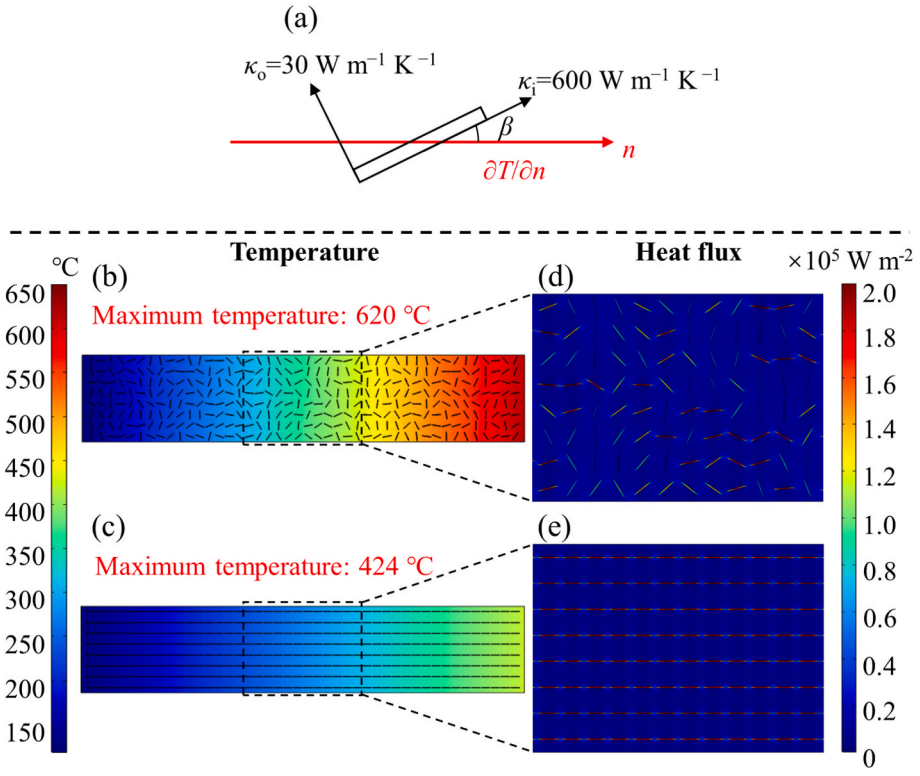

Fig. 8. Thermal analysis of composites with different hBN orientations. (a) Schematic of single hBN and the local temperature gradient. κ_o and κ_i are the out-plane and in-plane thermal conductivity of hBN, respectively. $\partial T/\partial n$ is the temperature gradient and n is the direction vector. β is the angle between hBN's in-plane direction and temperature gradient. Simualted temperature distribution of (b) composite with randomly distributed and (c) horizontally oriented hBN particles. Simulated heat flux distribution of (d) composite with randomly and (e) horizontally oriented hBN particles.

established on left side. The thermal conductivities of the PDMS matrix and the hBN filler were assigned as 0.15 W m^{-1} K^{-1} and 600 W m^{-1} K^{-1}, repectively. Under identical hBN loadings, composite-H exhibited a more uniform temperature distribution, and its maximum temperature was 424 °C, which was substantially lower than the value of 620 °C observed in composite-R, as depicted in Fig. 8b and c. Fig. 8d and e show

the comparison of the heat flux in the both composites. The high consistency with the direction of temperature gradients of horizontally oriented hBN contributed to a higher heat flux compared to that in hBN oriented in other dierction, where the disorganized alignment led to less efficient heat conduction enhancement. Specifically, horizontally oriented hBN maximised the heat conduction, demonstrating excellent ability on heat-flux manipulation. According to the results derived from the FEM analysis, the thermal conductivity of the composite was strongly influenced by the orientation of the hBN particles. Fig. 9a presents the in-plane thermal conductivity of the composites, which were 0.41, 0.92, 0.56, and 0.57 W m^{-1} K^{-1} for the randomly oriented, five-second spin coating, ten-second spin coating, and fifteen-second spin coating samples, respectively. The photos of the prepared composites (with a diameter of 25 mm and a thickness of 1 mm) are shown in Fig. 9c. Notably, the composites produced by spin coating exhibited higher thermal conductivities than those with random orientations, with the composite subjected to five-second spin coating achieving the highest conductivity. Fig. 9b contrasts the thermal conductivity of the composites farbricated using random orientation and five-second spin coating at hBN mass fraction of 5 wt%, 10 wt%, 15 wt%, and 20 wt%. As the mass fraction of hBN increases, the probability that particle collides with each other increases, which is unfavorable for the horizontal orientation of the particles. Under the same hBN mass fraction, the effect of particle collision on their orientation is the same across the whole spin coating process. Thus, the optimal duration of spin coating is applicable to the samples under different hBN mass fractions. The thermal conductivities of the composites produced by five-second spin coating were more than double those of randomly oriented composites across all tested mass fractions. This optimization and fabrication strategy has demonstrated considerable potential for effectively enhancing the thermal conductivity of TIMs, underscoring the critical role of particle orientation in the thermal performance of composites.

An experiment was designed to verify the heat dissipation ability of the composite prepared by five-second spin coating as shown in Fig. 10. In detail, a ceramic heating sheet (1.5 V, 1.5 W) with a diameter of 5 mm and a height of 0.6 mm, was placed to the center of samples (with a diameter of 25 mm and a height of 0.7 mm) to simulate a chip heat source. To ensure the samples and heat source were under the same pressure, polyphenylene sulfide (PPS) boards with bolts and nuts were adopted by supplying a torque of 15 N m. The surface temperature distribution of the samples was tested through a thermal infrared imager and the emissivity was set as 0.96. Fig. 10b shows the maximum surface temperature of the tested composite prepared by five-second spin coating with 10 wt% hBN (composite-H (10 wt%)) and the composite with randomly distributed hBN (composite-R (10 wt%)). When applied to the same chip heat source, composite-H (10 wt%) showed lower temperature on the surface compared to composite-R (10 wt%). Fig. 10c illustrates infrared images of the samples at 8 min. The temperature in the center of composite-H (10 wt%) is 9 ℃ lower due to the horizontally oriented hBN. FEM method was employed to simulate the temperature distribution of the experiment system, enabling thermal analysis of the heat source. Table 2 lists the parameters used for the simulation, the ambient temperature was set as 15 ℃, and all surfaces were set up for natural convection heat transfer (15 W m^{-2} K^{-1}). Fig. 10d illustrates the simulated temperature distributions of the top surfaces of PPS board and the tested samples. Comparing Fig. 10c and d, the simulated temperature distribution matches with the experiment, demonstrating the simulation is credible. Fig. 10e compares the temperature distribution of the heat source cooled by composite-H and composite-R. It can be found that the maximum temperature located on the surface of the ceramic heating sheet. Owing to the high in-plane thermal conductivity of composite-H, the T_{max} of the heat source is 24 ℃ lower than that of composite-R cooled heat source. The excellent in-plane heat-flux manipulating ability rapidly conducted the heat generated by the chip to the outside. These results demonstrated that the composite with horizontally oriented hBN owned a superior ability on the thermal management of the chip heat source.

5. Conclusion

In this study, we systematically developed a combined numerical and experimental methodology aimed at enhancing the thermal conductivity of TIMs through precisely controlled particle orientation. The numerical model focus on the orientation dynamics of disc-shaped particles within a fluid flow field during the spin coating process. The centrifugal force exerted by the spinning substrate induced a radial fluid flow, resulting in velocity gradients that influenced particle orientation. The particles underwent rotational motions aligned with the radial direction and oscillated in other directions. The Euler angle θ exhibited periodic variations due to the substantial shearing effect $\partial v_{ru}/\partial z$ in r-z plane and there was an equilibrium state that $\theta = 0$ or 180° which occupied greater proportion in a period. Thus, the horizontal orientation of the particle could be realized by optimizing the operational durations of spin coating to make most of the particles remain in equilibrium. Then, θ of 81 particles with different initial orientation at spin-coating durations of 5, 10, and 15 s were analyzed. The results showed that a spin coating duration of five seconds was optimal for achieving horizontal orientation, evidenced by HOP-2 of 29.63 % and HOP-5 of 67.90 %. Further, hBN-PDMS composites with a hBN mass fraction of 20 wt% were prepared, utilizing methods of random orientation and controlled spin coating for durations of five, ten and fifteen seconds. Angle distributions within these composites were quantitatively analyzed using an

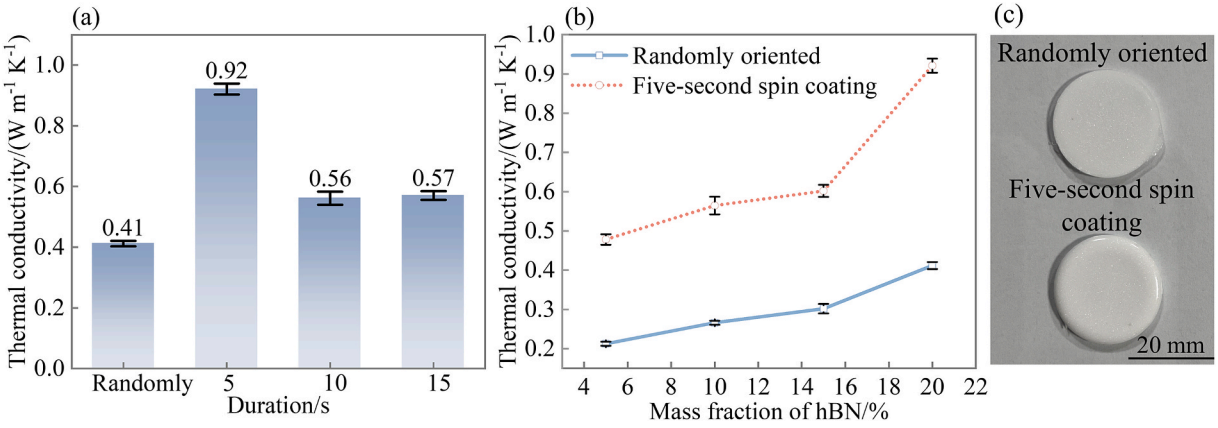

Fig. 9. Thermal conductivities of the prepared composites. (a) In-plane thermal conductivity of the composites prepared by randomly oriented, five-, ten-, and fifteen- second spin coating. (b) In-plane thermal conductivity of the composites prepared by randomly distributed and five-second spin coating with different hBN mass fractions. (c) Photos of the prepared composites.

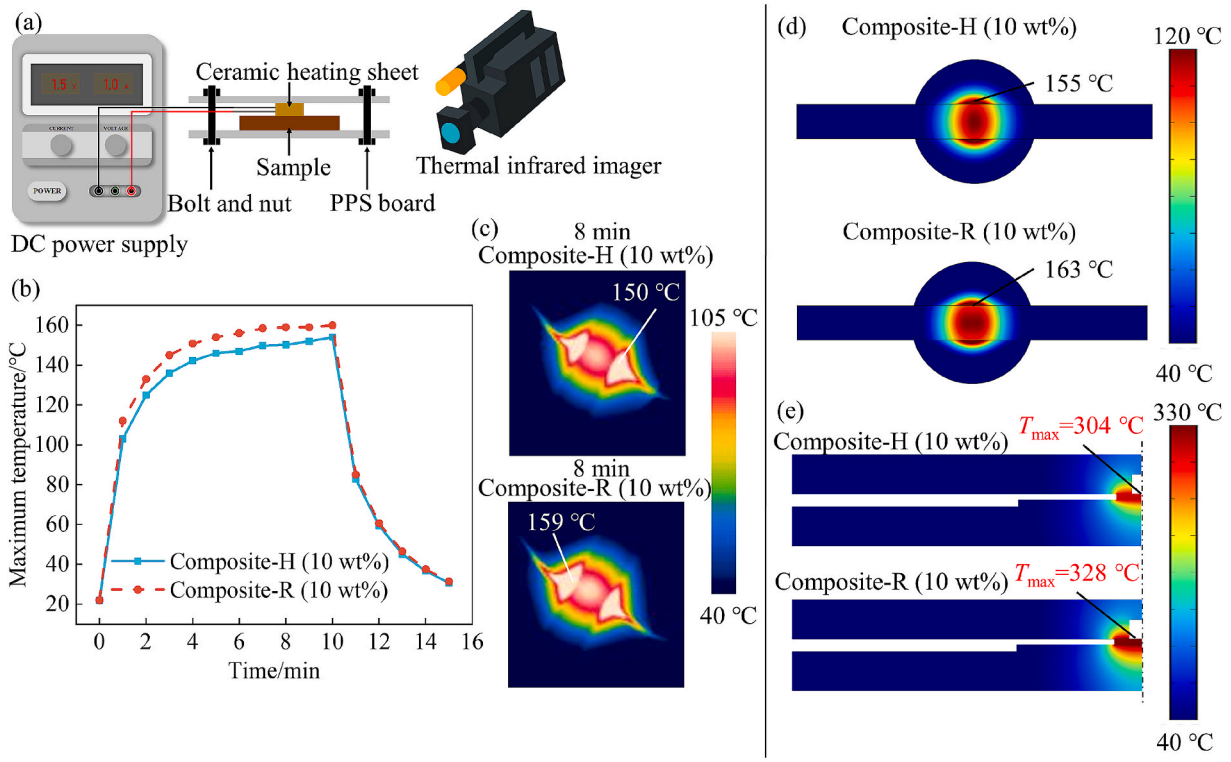

Fig. 10. Heat dissipation ability demonstration of composite-H (10 wt%). (a) Set up of the experiment to compare the heat dissipation ability of the samples. (b) Maximum surface temperature of composite-H (10 wt%) and composite-R (10 wt%) over time. (c) Infrared thermograms of the experiment. Simulated temperature distribution of (d) the top surface of the PPS board and tested samples, and (e) the vertical section of ceramic heating sheet and the tested samples.

Table 2
Parameters used for simulation. D is diameter, H is height, L is length, and W is width.

Components	Size mm	Thermal conductivity (W m^{-1} K^{-1})	Heat power W
Ceramic heating sheet	$D = 5$, $H = 0.6$	$\kappa = 30$	1.5
Composite-H	$D = 25$, $H = 0.7$	$\kappa_o = 0.56$, $\kappa_i = 0.15$	0
Composite-R	$D = 25$, $H = 0.7$	$\kappa = 0.25$	0
PPS board	$L = 71$, $W = 7$, $H = 4$	$\kappa = 0.25$	0

orientation algorithm based on microscale image identification. The sample prepared by five-second spin coating shows the highest HOP as 9.68 % of HOP-5, and 26.59 % of HOP-10 followed sequentially by fifteen-second, ten-second, and random orientation, which confirms the predictions of previous modeling and validates the model's accuracy. Mechnism of heat dissipation enhancement of anisotropic filler orientation control was revealed. The heat dissipation capacity is maximized when the in-plane orientation of hBN aligns with the temperature gradient. Thermal conductivities of the samples were measured, yielding values of 0.41, 0.92, 0.56, and 0.57 W m^{-1} K^{-1} for the randomly oriented, five-second spin coating, ten-second spin coating, and fifteen-second spin coating samples, respectively. These results affirmed that spin coating serves as an effective method for achieving horizontal alignment of hBN platelets within the matrix, substantially enhancing the in-plane thermal conductivity of the TIMs. Moreover, the duration of spin coating can be finely regulated according to the insights provided by the numerical model. This integrated methodology highlights the significant potential of particle orientation engineering in augmenting the functional properties of composite materials in thermal management applications.

CRediT authorship contribution statement

Xuan Yang: Writing – review & editing, Writing – original draft, Validation, Software, Methodology, Investigation, Formal analysis, Data curation, Conceptualization. **Xinfeng Zhang:** Writing – review & editing, Validation, Investigation, Formal analysis, Conceptualization. **Tianxu Zhang:** Validation, Supervision, Methodology, Conceptualization. **Linyi Xiang:** Visualization, Investigation, Data curation, Conceptualization. **Bin Xie:** Writing – review & editing, Project administration, Funding acquisition, Conceptualization. **Xiaobing Luo:** Writing – review & editing, Supervision, Project administration, Funding acquisition.

Declaration of competing interest

The authors declare the following financial interests/personal relationships which may be considered as potential competing interests: Bin Xie reports financial support was provided by National Natural Science Foundation of China. If there are other authors, they declare that they have no known competing financial interests or personal relationships that could have appeared to influence the work reported in this paper.

Acknowledgement

This work is supported by the National Natural Science Foundation of China (52106089).

Data availability

Data will be made available on request.

References

[1] Dai W, Wang Y, Li M, Chen L, Yan Q, Yu J, et al. 2D Materials-based thermal interface materials: structure, properties, and applications. Adv Mater 2024;36(37):2311335.

[2] Sheng J, Zhang Z, Pang Y, Cheng X, Zeng C, Xu J-B, et al. Balancing interfacial toughness and intrinsic dissipation for high adhesion and thermal conductivity of polymer-based thermal interface materials. ACS Appl Mater Interfaces 2024;16(45):62961–9.

[3] Deng C, Zhang X, Peng J, Yang X, Shang B, Luo X. $In_{51}Bi_{32.5}Sn_{16.5}@SiO_2$ microcapsules-based composite phase change materials with high thermal conductivity and heat storage density for electronics thermal management. J Storage Mater 2024;86:111432.

[4] Zeng C, Zeng X, Cheng X, Pang Y, Xu J, Sun R, et al. Design of thermal interface materials with excellent interfacial heat/force transfer ability via hierarchical energy dissipation. Adv Funct Mater 2024;34(41):2406075.

[5] Liu Y, Li J. A protocol to further improve the thermal conductivity of silicone-matrix thermal interface material with nano-fillers. Thermochim Acta 2022;708:179136.

[6] Xu K, Zhang Z, Wang Y, Li M, Chen Y, Kong X, et al. Sandwich-structured thermal interface materials with high thermal conductivity. ACS Appl Eng Mater 2024;2(6):1572–81.

[7] Cai W, Lu Y, Wang C, Li Q, Zheng Y. Aluminum/graphene thermal interface materials with positive temperature dependence. ACS Appl Mater Interfaces 2024;16(26):33993–4000.

[8] An L, An M, Yao B, Song J, Zhang X, Ma W. Unlocking the trade-off between intrinsic and interfacial thermal transport of boron nitride nanosheets by surface functionalization for advanced thermal interface materials. Adv Mater 2024. e2412137.

[9] Zhang B, Dou Z, Yuan R, He L, Xie Z, Li C, et al. General approach to hydrolysis resistive aluminum nitride and its high-performance thermal interface materials. ACS Appl Mater Interfaces 2024;16(45):62721–31.

[10] Cheng Y, Yang X, Han Z, Wu W, Luo X, Ruan X. Abnormal in-plane thermal conductivity anisotropy in bilayer α-phase tellurene. Int J Heat Mass Transf 2022;192:122908.

[11] Zhao Y, Zhang Z, Cai C, Zhou Z, Ling Z, Fang X. Vertically aligned carbon fibers-penetrated phase change thermal interface materials with high thermal conductivity for chip heat dissipation. Appl Therm Eng 2023;230:120807.

[12] Xie B, Zhao W, Luo X, Hu R. Alignment engineering in thermal materials. Mat Sci Eng R 2023;154:100738.

[13] Sun Y, Niu B, Cai H, Tian H, Li L, Zhuang Q, et al. High-orientation and shape-controllable thermal conductive composites based on dense packing and injection molding method. ACS Appl Polym Mater 2025;7(8):4708–15.

[14] Moore AL, Shi L. Emerging challenges and materials for thermal management of electronics. Mater Today 2014;17(4):163–74.

[15] Besharat F, Manteghian M, Gallone G, Lazzeri A. Electric field induced alignment of graphene oxide nanoplatelets in polyethersulfone matrix. Nanotechnology 2020;31(15):155701.

[16] Remillard EM, Zhang Q, Sosina S, Branson Z, Dasgupta T, Vecitis CD. Electric-field alignment of aqueous multi-walled carbon nanotubes on microporous substrates. Carbon 2016;100:578–89.

[17] Cheng S, Guo X, Tan P, Lin M, Cai J, Zhou Y, et al. Aligning graphene nanoplates coplanar in polyvinyl alcohol by using a rotating magnetic field to fabricate thermal interface materials with high through-plane thermal conductivity. Compos B Eng 2023;264:110916.

[18] Ryu JH, Yang SM, Lee JU, Kim JH, Yang SJ. Magnetic alignment of electrochemically exfoliated graphite in epoxy as a thermal interface material with high through-plane thermal conductivity. Carbon Lett 2022;32(6):1433–9.

[19] Lu W, Deng Q, Liu M, Ding B, Xiong Z, Qiu L. Coaxial wet spinning of boron nitride nanosheet-based composite fibers with enhanced thermal conductivity and mechanical strength. Nano-Micro Lett 2023;16(1):25.

[20] Chen G, Zhu Z, Lu Z, Wang W, Zhang S, He P, et al. Regulated the orientation of graphene nanoplatelets via flow field in material extrusion for enhancing thermal conductivity. Addit Manuf 2025;101.

[21] Zhang X, Xie B, Zhou S, Yang X, Fan Y, Hu R, et al. Radially oriented functional thermal materials prepared by flow field-driven self-assembly strategy. Nano Energy 2022;104:107986.

[22] Zhang X, Yang X, Fan Y, Hu R, Xie B, Luo X. 3D-programmable streamline guided orientation in composite materials for targeted heat dissipation. Int J Extreme Manuf 2024;7(2):025504.

[23] Zhou K, Yang W, He Z, Xiao M. Direct numerical simulation of concentration and orientation distribution of fibers in a mixing layer. Abstr Appl Anal 2013;2013:1–8.

[24] Emslie AG, Bonner FT, Peck LG. Flow of a viscous liquid on a rotating disk. J Appl Phys 1958;29(5):858–62.

[25] Zhang X, Ye Z, Yang X, Fan Y, Hu R, Xie B, et al. Quantitively evaluation of fillers' alignment for targeted manufacturing of functional composite materials. Polym Compos 2023;45(1):653–67.